ROYAL SOCIETY OF CHEMISTRY

PAPER

Check for updates

Hydrogen-bonded organic framework with tailored pores prepared by enlarging the core size for high-performance Xe/Kr separation†

Zhen Yuan, Liangji Chen, Xin Zhou, Lu Li, Yunbin Li, Yisi Yang, Zhiqi Zhou, Yanting Chen, Shengchang Xiang, [ID] Banglin Chen [ID] and Zhangjing Zhang [ID] *

The efficient separation of xenon (Xe) and krypton (Kr) mixtures is a valuable but challenging process in the gas industry. Hydrogen-bonded organic frameworks (HOFs) have emerged as a promising class of porous materials for gas separation; however, due to the lack of available design methods, accurately adjusting the pore size of HOFs to improve the separation performance remains a major challenge. Herein, we present a pore engineering optimized strategy by enlarging the core size of the rigid monomers to increase the pore size of benzene cyanide-based HOFs. The replacement of the benzene ring in the molecular core of HOF-40 with a larger-sized dipyrrole ring resulted in the assembly of HOF-FJU-8a with a slightly larger pore size of 4.2×4.6 Å^2, which is demonstrated as the highest performing HOF material for Xe/Kr separation reported to date. The superior Xe/Kr separation was determined by the gas adsorption and dynamic breakthrough experiments, showing a separation factor of 8.5 and a Kr productivity over 72 L kg^{-1} from the binary Xe/Kr mixture. The tailored pore size of HOF-FJU-8a played a crucial role in enabling the significant differential host–guest interactions and binding affinity, as confirmed by the single crystal structures of Xe- or Kr-loaded HOF-FJU-8a and GCMC calculations.

Introduction

The noble gases xenon (Xe) and krypton (Kr) are commercially valuable commodities with broad applications encompassing areas, such as spacecraft propellants, nuclear energy, lasers, medical devices, and other fundamental research endeavors.[1–4] The industrial production of Xe and Kr is through the cryogenic distillation of air, generating a byproduct of the Xe/Kr mixture (20 : 80, v/v) and requiring an energy-intensive distillation purification process to manufacture high-purity Xe and Kr.[5,6] Recently, gas separation strategies utilizing porous solid adsorbents, such as metal–organic frameworks (MOFs), covalent organic frameworks (COFs), and organic cages, have emerged as a promising alternative method owing to their low cost, milder operation conditions, and energy-saving prospects.[7–15] However, due to the absence of dipole or quadrupole moments in both Xe and Kr, along with their closely matched kinetic diameters (Xe, 4.047 Å and Kr, 3.655 Å),[16] the exploration of porous adsorbents with controllable structures to balance the capability and selectivity remains a captivating and demanding project.

Hydrogen-bonded organic frameworks (HOFs) have emerged as a highly promising class of porous materials due to their well-defined pore features, extensive structural tunability, multi-functionalities, good solution processability, and easy regeneration.[17–20] The design of HOFs can be achieved by altering the combination of the cores of monomer molecules and hydrogen-bonding linkers.[21] Up to now, various H-bonding linkers have been explored for the assembly of HOFs, such as carboxylic acid,[22,23] 2,4-diaminotriazine,[24,25] pyrazole,[26,27] pyridine,[28,29] aldehyde,[30,31] and benzene cyanide.[32,33] The benzene cyanide linker is currently attracting considerable attention owing to its ability to provide multiple hydrogen-bonding nodes, and to confer excellent stability and ultramicroporous environment. Indeed, the bright potential of benzene cyanide-based HOFs have been demonstrated in various crucial applications, such as gas adsorption and separation,[34–37] fluorescence sensing,[38,39] laser,[40] and molecular recognition.[41,42]

We have recently reported a benzene cyanide-based HOF-40 (ref. 43) with a pore size of 3.8 Å based on 1,2,4,5-tetrakis(4-cyanophenyl)benzene, which exhibited the highest IAST selectivity for Xe/Kr separation among all the HOFs reported to date.[44,45] Notably, the pore size of HOF-40 is relatively smaller than the kinetic diameter of Xe (4.0 Å).[16] In principle,[46,47] HOF-40 should only adsorb Kr and exclude Xe, but the actual results demonstrate preferential adsorption for Xe over Kr due to the

Fujian Key Laboratory of Polymer Materials, College of Chemistry and Materials Science, Fujian Normal University, Fuzhou, 350007, Fujian, China. E-mail: zzhang@fjnu.edu.cn

This journal is © The Royal Society of Chemistry 2023

J. Mater. Chem. A, 2023, 11, 21857–21863 | 21857

higher polarizability of Xe. The inconsistency between experimental results and theory inspires us to further explore the optimal pore size of adsorbents that is more suitable for the separation of Xe/Kr. However, it is a pity that the pore engineering optimization strategies for HOFs are very limited.[48–50] How to precisely tune the pore size of HOFs to achieve enhanced separation performance remains a significant challenge.

Herein, we propose the enlargement of the core size of rigid monomers to increase the pore size of benzene cyanide-based HOFs, aiming at optimizing and regulating the Xe/Kr separation performance (Scheme 1). The benzene ring in the molecular core of HOF-40 was replaced with a larger-sized dipyrrole ring, resulting in the assembly of HOF-FJU-8a with a slightly larger pore size of 4.6×4.2 Å^2. HOF-FJU-8a demonstrates a remarkable Xe adsorption capacity of 1.81 mmol g^{-1} and outstanding selectivity of 12.1, as evidenced by the sorption isotherms. The efficiency of Xe/Kr separation was further confirmed through dynamic breakthrough curves, showing a separation factor of 8.5 and a Kr productivity of 72 L kg^{-1} with a purity of $\geq$ 99.5%, which is much superior to those of HOF-40 with a separation factor of 2.5 and Kr productivity of 44.4 L kg^{-1}. Single-crystal X-ray diffraction and theoretical calculations highlight the importance of tailored pore environments within confined channels.

Results and discussion

In HOF-FJU-8a[36] (ESI Table S1†), half of two crystallographically independent 4,4′,4″,4‴-(pyrrolo[3,2-b]pyrrole-1,2,4,5-tetrayl) tetrabenzonitrile (DP-4CN) linkers in the asymmetric unit and one of the linkers (linker 1) is linked to four neighboring linkers to form a single network involving C–H⋯N hydrogen bonds with C⋯N distances of 3.328 Å (C6–H6⋯N1) and 3.597 Å (C16–H16⋯N2) (Fig. 1a). The formed two-dimensional (2D) layer demonstrates a void of 5.8×5.2 Å^2 along the ac plane and the 2D layers are further connected by another linker (linker 2) through multiple D–A π⋯π interactions with distances of 3.505 and 3.710 Å (Fig. 1b). With the connection of linker 2, the voids in the 2D layers are further narrowed down and the final structure possesses a 3D framework containing narrow 1D channels $ca.$ 4.2×4.6 Å^2 along the crystallographic b-axis direction (Fig. 1c and the ESI Fig. S1†). With the enlarged core size from the benzene ring in HOF-40 to the dipyrrole ring in HOF-FJU-8a, the aperture size of HOF-FJU-8a is slightly larger

than that of HOF-40 (ref. 43) (3.8×4.1 Å^2), which may have the potential to balance the selectivity and adsorption capacity for Xe/Kr separation.

The purity of the as-synthesized HOF-FJU-8a was confirmed by powder X-ray diffraction (PXRD), which exhibited a strong agreement between the simulated and experimental patterns (Fig. S2†). The chemical structure of HOF-FJU-8a was verified using Fourier transform infrared (FTIR) and ^{1}H-NMR spectra (Fig. S3 and S4†). Furthermore, in the thermogravimetric analysis (TGA), no significant weight loss was observed before reaching 350 °C, indicating the absence of solvent molecules in the pore channels and confirming the successful activation of HOF-FJU-8a (Fig. S5†). The permanent porosity of HOF-FJU-8a was demonstrated from the N$_2$ adsorption isotherm at 77 K, which revealed a Brunauer–Emmett–Teller (BET) surface area of 375 m^2 g^{-1} (Fig. S6a†). The pore size distribution (PSD) of HOF-FJU-8a was analyzed using the isotherms of 273 K CO$_2$ and 77 K N$_2$ based on the nonlocal density functional theory (NLDFT) model, which showed a narrow PSD with peaks at 5.7, 9.6, and 18.5 Å (Fig. S6b†). Motivated by the favorable pore size of the HOF-FJU-8a structure, we conducted single-component adsorption isotherms to assess its adsorption capabilities for Xe and Kr (Fig. 2a). Notably, the adsorption isotherm of Xe exhibited a significantly steeper increase than that of Kr in the low-pressure region. At 1 bar, the Xe uptake capacities for HOF-FJU-8a were 2.03 mmol g^{-1} and 1.81 mmol g^{-1} at 273 K and 296 K, respectively. In contrast, the Kr uptakes were found to be 1.17 mmol g^{-1} and 0.77 mmol g^{-1} at the same conditions, respectively. This distinct difference in the adsorption capacities for Xe and Kr suggests the potential of HOF-FJU-8a for Xe/Kr separation. Furthermore, at 296 K and 1 bar, the Xe uptake capacity of HOF-FJU-8a surpassed that of HOF-40 (1.56 mmol g^{-1})[43] and HIAM-103 (1.39 mmol g^{-1}),[45] as well as those of many MOFs such as Ni(4-DPDS)$_2$CrO$_4$ (1.61 mmol g^{-1}),[51] Co$_3$(OH)$_2$(C$_4$O$_4$)$_2$ (1.35 mmol g^{-1}),[52] and FJU-55 (1.41 mmol g^{-1}),[53] and was comparable to those of some benchmark materials including 1-Zn (2.16 mmol g^{-1}),[13] CROFOUR-1-Ni (1.77 mmol g^{-1}),[54] and NU-403 (1.70 mmol g^{-1}).[55] Particularly, the packing density of Xe in HOF-FJU-8a reached an impressive value of up to 1397 g L^{-1} under ambient conditions, as determined by the adsorption capacity and theoretical pore volume. This value is approximately 237 times higher than that of gaseous Xe (5.89 g L^{-1} at 1 bar and 273 K) and about half of that of liquid Xe (3057 g L^{-1} at 1 atm and 165 K), implying the efficient packing of Xe molecules within the channels of HOF-FJU-8a.

To further estimate the gas affinity, we calculated the adsorption heats (Q_{st}) for Xe and Kr using the virial method based on the isotherms measured at 273 K and 296 K (Fig. S7 and S8†). As illustrated in Fig. 2b, the corresponding Q_{st} value of HOF-FJU-8a for Xe was determined to be 30.6 kJ mol^{-1} at nearly zero coverage, which is significantly higher than that of Kr (12.1 kJ mol^{-1}). This observation indicates a stronger affinity between Xe and the host framework, which is consistent with the results obtained from the sorption isotherms. Notably, compared to HOF-40 (Q_{st} (Xe) = 32.8, Q_{st} (Kr) = 24.4), HOF-FJU-8a with a slightly larger pore size not only retains the high Q_{st} for Xe but also significantly reduces the affinity for Kr. The

Scheme 1 Schematic diagram of optimized pore engineering of benzene cyanide-based linker-based HOFs for enhanced Xe/Kr separation by enlarging the core size of the rigid monomer.

21858 | *J. Mater. Chem. A*, 2023, **11**, 21857–21863

This journal is © The Royal Society of Chemistry 2023

Fig. 1 Crystal structure of HOF–FJU–8a. (a) The self–assembled 2D layer from "linker 1" by C≡N⋯H−C dimers viewed along the *b* axis. (b) The 2D layers are connected by "linker 2" *via* D−A π⋯π interactions to form a 3D framework, which shows 1D channels of 4.2 × 4.6 Å² along the *b* axis (c). "Linker 1", grey, carbon; blue, nitrogen; white, hydrogen; "Linker 2", red color.

difference in the adsorption heats (ΔQ, calculated as Q_{st} (Xe) − Q_{st} (Kr)) of HOF-FJU-8a reaches 15 kJ mol^{-1}, which is surpassed only by a few MOFs, such as SMOF-PFSIX-1a,[56] FJU-55,[53] and ZJU-74a-Ni,[8] and exceeds the majority of other reported porous materials (Fig. S9 and Table S2†), showing a significant affinity difference for Xe and Kr.

The adsorption selectivity of HOF-FJU-8a for the byproduct of a Xe/Kr mixture (20/80) in commercial cryogenic fractional air distillations[8,55] was predicted using the ideal adsorbed solution theory (IAST) (Fig. S10 and S11†). As illustrated in Fig. 2c, the Xe/Kr selectivity ranges from 13.8 to 12.1 as the pressure increases from 0 to 100 kPa at 296 K, which is comparable to that of some benchmark adsorbents[3,57–59] and higher than that of the majority of porous materials,[56,60–64] demonstrating

a balanced performance in terms of both uptake and separation selectivity (Fig. S12†). Additionally, the Henry selectivity was also calculated derived from the Xe and Kr sorption isotherms at low pressure (Fig. S13†). The Henry coefficient of HOF-FJU-8a was determined to be 10.9 at 296 K, indicating strong adsorption of Xe and suggesting the potential for efficient Xe/Kr separation under low-pressure conditions. The comparison of the reported pore sizes of HOF structures with the IAST selectivity revealed a clear volcano-shaped curve (Fig. 2d). There is a corresponding increase in IAST selectivity with the pore size slightly increasing from 3.8 Å in HOF-40 to 4.2 Å in HOF-FJU-8a, and the further augmentation of the pore size to 6 Å (HIAM-103) and even 12 Å (HOF-BTB) results in a substantial decline in IAST. This observation suggests that a pore size range of 4–5 Å

Fig. 2 (a) Xe and Kr adsorption isotherms of HOF–FJU–8a at 273 K and 296 K. (b) Heat of adsorption (Q_{st}) curves of HOF–FJU–8a for Xe and Kr. (c) IAST selectivity of Xe/Kr (20/80) at 296 K. (d) Comparison of the pore size and IAST selectivity of HOF–FJU–8a with other reported HOF materials. Dynamic breakthrough curves (e) and the cycling breakthrough experiments (f) of HOF–FJU–8a for Xe/Kr (20/80) gas mixture under 296 K and 1 bar, at a flow rate of 2.0 mL min^{-1}. (g) Comparison of the separation factor and Kr productivity of HOF–FJU–8a with other reported HOF materials.
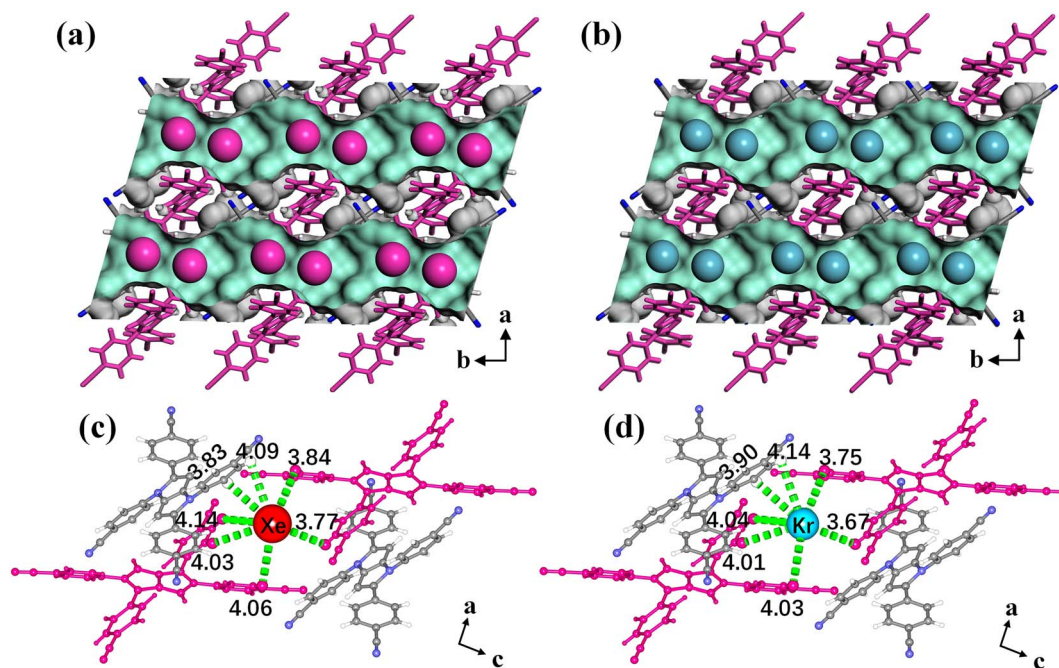
Fig. 3 The gas-loaded structures of HOF-FJU-8a·Xe (a) and HOF-FJU-8a·Kr (b). Binding sites for Xe (c) and Kr (d) uptake and their close contacts with the framework fragments.

may be favorable for the separation of Xe/Kr in HOFs and highlights HOF-FJU-8a as the optimal HOF material for this challenging separation.

To evaluate the practical separation performance of HOF-FJU-8a, a laboratory-scale dynamic column breakthrough experiment was conducted using a binary Xe/Kr mixture (20 : 80) at 296 K and 1 bar, at a flow rate of 2 mL min^{-1} (Fig. S14†). As depicted in Fig. 2e, the gas mixtures passing through the packed column can be effectively separated. Due to the weaker affinity of the HOF-FJU-8a framework for Kr, Kr is rapidly expelled from the framework and elutes first from the fixed bed at 4 min g^{-1}, while Xe is preferentially adsorbed within the channels of HOF-FJU-8a and is not detected until 40 min g^{-1}, demonstrating the ultra-long retention time of HOF-FJU-8a. Based on the breakthrough curve, the dynamic Xe capture capacity (q_{Xe}) and separation factor ($\alpha_{Xe/Kr}$) were determined to be 1.02 mmol g^{-1} and 8.5, respectively (Fig. S15†). Moreover, the productivity of high-purity Kr ($\geq$99.5%) can reach up to 72 L kg^{-1} under a given cycle (Fig. S16†), which is much higher than that observed on HOF-40 (44.4 L kg^{-1}). To further investigate the recyclability of HOF-FJU-8a for Xe/Kr separation, we conducted three cycles of mixed gas dynamic breakthrough experiments (Fig. 2f). The results demonstrate that HOF-FJU-8a maintained the same breakthrough time and dynamic capture amount of Xe as in the initial cycle (Fig. S17†). Furthermore, the PXRD patterns confirm that HOF-FJU-8a still retains its intact structure after the dynamic breakthrough experiments (Fig. S18†). FTIR spectra confirm its good chemical structure stability (Fig. S19†). These findings provide solid evidence that HOF-FJU-8a can achieve efficient separation of Xe from the binary Xe/Kr mixture under dynamic conditions, highlighting it as the highest

performing HOF material for Xe/Kr separation reported to date (Fig. 2g). Furthermore, although the separation performance is lower than that of the benchmark ZJU-74a-Ni[8] and MOF-Cu–H,[57] it is comparable to that of HOF-ZJU-201a,[10] and superior to those of most absorbents[13,52,53,56,59,62] (Fig. S20†).

Single-crystal X-ray diffraction (SCXRD) measurements of Xe/Kr-loaded HOF-FJU-8a were carried out to gain structural insights into the binding conformations and host–guest interactions. The data for HOF-FJU-8a·1Xe and HOF-FJU-8a·0.56Kr were collected at 150 K (Table S1†). The SCXRD results reveal that the loaded Xe and Kr in the framework exhibit noticeable anisotropy and relative disorder, presenting a banded distribution within the 1D channels. However, both Xe and Kr exhibited a preference for occupying the central positions adjacent to the pore constrictions, demonstrating similar adsorption locations (Fig. 3a and b). The locations of Xe and Kr within the HOF-FJU-8a framework were further verified through the density distribution from grand canonical Monte Carlo (GCMC) simulations. As illustrated in Fig. S21,† despite the banded distribution of density within the pores, the density of Xe and Kr was significantly higher near the pore constrictions. The density of Xe is noticeably higher than the corresponding Kr, which aligns with the higher uptake amount of Xe as compared with Kr observed from the adsorption isotherms. The calculated binding energy for Xe is 7.3 kcal mol^{-1}, which is in good agreement with the low coverage isosteric heat of adsorption, and it is significantly higher than that of Kr (5.3 kcal mol^{-1}).

To further understand the host–guest interactions, we calculated the Hirshfeld surface[65] of Xe and Kr within the pore channels. As depicted in Fig. S22 and S23,† the hydrogen atoms

21860 | J. Mater. Chem. A, 2023, 11, 21857–21863

This journal is © The Royal Society of Chemistry 2023

exhibited the most significant contact contribution with Xe and Kr, accounting for 71.4% and 74.8%, respectively. The contact area between carbon atoms and Xe/Kr is merely 21.5%/17.0%, whereas the contact-involving nitrogen atoms is almost negligible. This demonstrates the crucial role played by the hydrogen sites within the pore channels of HOF-FJU-8a in facilitating host–guest interactions. According to the SCXRD results, the Xe atom is surrounded by seven hydrogen atoms to form multiple van der Waals interactions (Fig. 3c), involving five Xe···H interactions (ranging from 3.84 to 4.14 Å) between Xe and hydrogen atoms on the benzene rings of the linker 2, as well as two Xe···H interactions (3.83 and 4.09 Å) originating from the benzene rings of linker 1. The interactions between Kr and the framework are similar to those of Xe, with Kr···H interactions ranging from 3.67 to 4.14 Å (Fig. 3d). Despite this distance range is similar to Xe···H interactions, the Xe···H distance is even closer to the sum of the van der Waals radii of Xe and H. Furthermore, the unit cell volume shrinks by 0.6% in the Xe-loaded structure in contrast with the guest-free HOF-FJU-8a, while the Kr-loaded structure only shrinks by 0.3% (ESI Table S1†), revealing a stronger affinity of HOF-FJU-8a with Xe rather than Kr. The above results confirm that the appropriate pore size of HOF-FJU-8a enhances the differences in the host–guest interactions and binding affinity between Xe and Kr within the framework, which enables the achievement of efficient adsorption and separation of the xenon and krypton mixtures.

Conclusions

In conclusion, we have demonstrated that the modulation of molecular core size is an effective pore engineering optimized strategy for enhancing the gas separation performance of HOFs. The pore size of 4.2×4.6 Å^2 in HOF-FJU-8a provides a significant differentiation in the adsorption and binding affinity of Xe and Kr, resulting in superior separation performance compared with all previously reported HOFs. Our study also indicates that the HOF pore size range of 4–5 Å may be suitable for efficient Xe/Kr separation, as confirmed by the modelling studies and column breakthrough experiments. This study unveils that the appropriate pore environment in HOFs through the rational design of monomer molecules can achieve efficient gas separation, which may offer valuable insights for designing HOFs to address the challenging separation tasks.

Experimental

Materials and methods

All reagents and solvents used in the synthetic studies were commercially available and were used as supplied without further purification. Powder X-ray diffraction (PXRD) patterns were recorded on a PANalytical X'Pert³ powder diffractometer equipped with a Cu-sealed tube ($\lambda = 1.54184$ Å) at 40 kV and 40 mA. Single crystal X-ray diffraction data were collected at 150 K on an XtaLAB Synergy R, HyPix diffractometer. The simulated pattern was produced using the Mercury V1.4 program and single-crystal diffraction data. FTIR spectra were recorded using a Thermo Nicolet 5700 FTIR spectrometer in the range of 400–4000 cm^{-1} (KBr pellets). ^{1}H-NMR spectra were recorded on a Bruker Advance 400 MHZ spectrometer. TGA was performed on a METTLER TGA/SDTA 851 thermal analyzer at a heating rate of 10 °C min^{-1} from 30 to 600 °C under N$_2$ atmosphere.

Synthesis of HOF-FJU-8a

HOF-FJU-8a was obtained according to our previous report (Scheme S1†).[36] Firstly, the guest-containing structure HOF-FJU-8 was obtained by simple crystallization of DP-4CN from its dimethyl sulfoxide solution. The fresh sample of HOF-FJU-8 was guest-exchanged with ethanol 12 times in a 4 °C refrigerator (once an hour), and then filtered and degassed at 60 °C for 1 day to obtain the guest-free HOF-FJU-8a.

The Xe/Kr loaded HOF-FJU-8a was prepared by the following steps. After the single-crystal data collection for guest-free HOF-FJU-8a at 150 K, the single-crystal HOF-FJU-8a and its loaded crystal carrier were placed into a conical flask, and a layer of tin foil was wrapped around the crystal carrier to protect the single crystal. The upper part of the conical flask was connected with a three-way glass valve. The system was filled with Xe or Kr through ASAP 2020 HD88, and the pressure was measured to be 1 atm. The system was left standing for 8 h to ensure the adsorption balance of single crystal for gas, and then quickly transferred to the single crystal diffractometer for testing and was kept at 150 K during data collection for HOF-FJU-8a·Xe and HOF-FJU-8a·Kr.

Gas adsorption measurements

Gas adsorption isotherms on the guest-free sample (HOF-FJU-8a) were measured on a Micromeritics ASAP 2020 HD88 surface area analyzer, and a circulating bath with a mixed aqueous solution of ethylene glycol and water was used to control the test temperature (273 and 296 K).

Breakthrough experiment

The breakthrough experiments for Xe/Kr mixtures were carried out at an ABR breakthrough equipment (Hiden, UK). In a typical experiment, the activated HOF-FJU-8a (0.62 g) powder was packed into a stainless steel HPLC column (4.6 mm I.D. × 50 mm). A stream of He flow at a flow rate of 10.0 mL min^{-1} was introduced into the column for 1 hour to further purge the materials before measuring the breakthrough experiments. The experimental breakthrough experiments were under the flow of a gas mixture of Xe/Kr (20/80, v/v). The mixed gas was introduced at a constant flow rate of 2.0 mL min^{-1} at 296 K, and the outlet gas passing through the column was analysed using a Hiden HPR-20 EGA mass spectrometer for continuous sampling gas analysis.

Grand canonical Monte Carlo (GCMC) simulations

Grand canonical Monte Carlo (GCMC) calculations were performed using the Materials Studio' Sorption modules to calculate the energy and density distribution of Xe and Kr adsorbed on the HOF-FJU-8a. A $3 \times 3 \times 3$ crystallographic unit cell was used for GCMC simulation, and a total of 1×10^6 equilibration

This journal is © The Royal Society of Chemistry 2023

J. Mater. Chem. A, 2023, **11**, 21857–21863 | **21861**

steps and 1×10^6 production steps were set for the simulation. A rigid framework assumption was used in all simulations. In addition, the simulations were also carried out at 298 K, adopting the fixed loading task, the Metropolis method in the sorption module, and the Universal forcefield (UFF). The interaction energy between the guest molecule (Xe or Kr) and the framework was computed through the Coulomb and Lennard-Jones 6–12 (LJ) potentials. The cutoff radius was chosen as 18.5 Å for the LJ potential, and the long-range electrostatic interactions were handled using the Ewald and group summation method.

Hirshfeld surface calculations

Hirshfeld surface calculations were performed using the CrystalExplorer program.[65] When the CIF files of HOF-FJU-8a·Xe and HOF-FJU-8a·Kr were read into the CrystalExplorer program, all bond lengths to hydrogen were automatically modified to the typical standard neutron values (C–H = 1.083 Å and N–H = 1.009 Å). In this study, all Hirshfeld surfaces were generated using a very high surface resolution with the mapped 3D d_{norm} surfaces.

Author contributions

Zhen Yuan conducted the experiments. Liangji Chen, Xin Zhou, Lu Li, Yunbin Li, Yisi Yang, Zhiqi Zhou, and Yanting Chen conducted data collection. Zhen Yuan, Shengchang Xiang, Banglin Chen, and Zhangjing Zhang wrote the manuscript and discussed the results with all authors.

Conflicts of interest

There are no conflicts to declare.

Acknowledgements

Notes and references

1 G. A. Lane, M. L. Nahrwold, A. R. Tait, M. Taylor-Busch, P. J. Cohen and A. R. Beaudoin, *Science*, 1980, **210**, 899–901.

2 D. Banerjee, A. J. Cairns, J. Liu, R. K. Motkuri, S. K. Nune, C. A. Fernandez, R. Krishna, D. M. Strachan and P. K. Thallapally, *Acc. Chem. Res.*, 2015, **48**, 211–219.

3 L. Chen, P. S. Reiss, S. Y. Chong, D. Holden, K. E. Jelfs, T. Hasell, M. A. Little, A. Kewley, M. E. Briggs, A. Stephenson, K. M. Thomas, J. A. Armstrong, J. Bell, J. Busto, R. Noel, J. Liu, D. M. Strachan, P. K. Thallapally and A. I. Cooper, *Nat. Mater.*, 2014, **13**, 954–960.

4 D. Banerjee, C. M. Simon, S. K. Elsaidi, M. Haranczyk and P. K. Thallapally, *Chem*, 2018, **4**, 466–494.

5 S. U. Nandanwar, K. Coldsnow, V. Utgikar, P. Sabharwall and D. Eric Aston, *Chem. Eng. J.*, 2016, **306**, 369–381.

6 D. S. Sholl and R. P. Lively, *Nature*, 2016, **532**, 435–437.

7 S. Chu, Y. Cui and N. Liu, *Nat. Mater.*, 2017, **16**, 16–22.

8 J. Pei, X.-W. Gu, C.-C. Liang, B. Chen, B. Li and G. Qian, *J. Am. Chem. Soc.*, 2022, **144**, 3200–3209.

9 H. Kim, J. H. Choe, M. Kang, D. W. Kang, H. Yun, J. Youn, W.-G. Lee, J.-H. Lee and C. S. Hong, *Small*, 2023, 2301905.

10 Y. Liu, H. Wu, L. Guo, W. Zhou, Z. Zhang, Q. Yang, Y. Yang, Q. Ren and Z. Bao, *Angew. Chem., Int. Ed.*, 2022, **61**, e202117609.

11 M. Miklitz, S. Jiang, R. Clowes, M. E. Briggs, A. I. Cooper and K. E. Jelfs, *J. Phys. Chem. C*, 2017, **121**, 15211–15222.

12 Z. Jia, Z. Yan, J. Zhang, Y. Zou, Y. Qi, X. Li, Y. Li, X. Guo, C. Yang and L. Ma, *ACS Appl. Mater. Interfaces*, 2021, **13**, 1127–1134.

13 W.-L. Shan, M.-L. Xu, H.-H. Hou, P. Zhao, Q.-Y. Zhang, M.-J. Yin and F. Luo, *Nano Res.*, 2023, **16**, 2536–2542.

14 C. Ji, K. Su, W. Wang, J. Chang, M. El-Sayed El-Sayed, L. Zhang and D. Yuan, *CCS Chem.*, 2021, **4**, 3095–3105.

15 F. Qiu, X. Chen, W. Wang, K. Su and D. Yuan, *CCS Chem.*, 2023, DOI: **10.31635/ccschem.31023.202302903**.

16 J.-R. Li, R. J. Kuppler and H.-C. Zhou, *Chem. Soc. Rev.*, 2009, **38**, 1477–1504.

17 Z. Zhang, Y. Ye, S. Xiang and B. Chen, *Acc. Chem. Res.*, 2022, **55**, 3752–3766.

18 X. Song, Y. Wang, C. Wang, D. Wang, G. Zhuang, K. O. Kirlikovali, P. Li and O. K. Farha, *J. Am. Chem. Soc.*, 2022, **144**, 10663–10687.

19 B. Wang, R.-B. Lin, Z. Zhang, S. Xiang and B. Chen, *J. Am. Chem. Soc.*, 2020, **142**, 14399–14416.

20 Z.-J. Lin, S. A. R. Mahammed, T.-F. Liu and R. Cao, *ACS Cent. Sci.*, 2022, **8**, 1589–1608.

21 R.-B. Lin, Y. He, P. Li, H. Wang, W. Zhou and B. Chen, *Chem. Soc. Rev.*, 2019, **48**, 1362–1389.

22 Q. Yin, E. V. Alexandrov, D.-H. Si, Q.-Q. Huang, Z.-B. Fang, Y. Zhang, A.-A. Zhang, W.-K. Qin, Y.-L. Li, T.-F. Liu and D. M. Proserpio, *Angew. Chem., Int. Ed.*, 2022, **61**, e202115854.

23 T. Hashimoto, R. Oketani, M. Nobuoka, S. Seki and I. Hisaki, *Angew. Chem., Int. Ed.*, 2023, **62**, e202215836.

24 Y. He, S. Xiang and B. Chen, *J. Am. Chem. Soc.*, 2011, **133**, 14570–14573.

25 P. Li, Y. He, Y. Zhao, L. Weng, H. Wang, R. Krishna, H. Wu, W. Zhou, M. O'Keeffe, Y. Han and B. Chen, *Angew. Chem., Int. Ed.*, 2015, **54**, 574–577.

26 T.-H. Chen, I. Popov, W. Kaveevivitchai, Y.-C. Chuang, Y.-S. Chen, O. Daugulis, A. J. Jacobson and O. Š. Miljanić, *Nat. Commun.*, 2014, **5**, 5131.

27 M. I. Hashim, H. T. M. Le, T.-H. Chen, Y.-S. Chen, O. Daugulis, C.-W. Hsu, A. J. Jacobson, W. Kaveevivitchai, X. Liang, T. Makarenko, O. Š. Miljanić, I. Popovs, H. V. Tran, X. Wang, C.-H. Wu and J. I. Wu, *J. Am. Chem. Soc.*, 2018, **140**, 6014–6026.

28 Y. Lv, J. Liang, Z. Xiong, H. Zhang, D. Li, X. Yang, S. Xiang and Z. Zhang, *Chem. – Eur. J.*, 2023, **29**, e202204045.

21862 | *J. Mater. Chem. A*, 2023, **11**, 21857–21863

This journal is © The Royal Society of Chemistry 2023

29 Y. Lv, Z. Xiong, Y. Li, D. Li, J. Liang, Y. Yang, F. Xiang, S. Xiang, Y. S. Zhao and Z. Zhang, *J. Phys. Chem. Lett.*, 2022, **13**, 130–135.

30 L. Chen, Z. Yuan, H. Zhang, Y. Ye, Y. Yang, F. Xiang, K. Cai, S. Xiang, B. Chen and Z. Zhang, *Angew. Chem., Int. Ed.*, 2022, e202213959.

31 L. Hou, C. Shan, Y. Song, S. Chen, L. Wojtas, S. Ma, Q. Sun and L. Zhang, *Angew. Chem., Int. Ed.*, 2021, **60**, 14664–14670.

32 M. C. Das, S. C. Pal and B. Chen, *Joule*, 2022, **6**, 22–27.

33 F. Xie, H. Wang and J. Li, *Matter*, 2022, **5**, 2516–2518.

34 Y. Yang, L. Li, R.-B. Lin, Y. Ye, Z. Yao, L. Yang, F. Xiang, S. Chen, Z. Zhang, S. Xiang and B. Chen, *Nat. Chem.*, 2021, **13**, 933–939.

35 Y. Yang, H. Zhang, Z. Yuan, J.-Q. Wang, F. Xiang, L. Chen, F. Wei, S. Xiang, B. Chen and Z. Zhang, *Angew. Chem., Int. Ed.*, 2022, **61**, e202207579.

36 Z. Yuan, X. Jiang, L. Chen, J. Chen, L. Li, Y. Yang, Y. Li, F. Xiang, S. Xiang, B. Chen and Z. Zhang, *CCS Chem.*, 2023, DOI: 10.31635/ccschem.31023.202302840.

37 Y. Chen, Y. Yang, Y. Wang, Q. Xiong, J. Yang, S. Xiang, L. Li, J. Li, Z. Zhang and B. Chen, *J. Am. Chem. Soc.*, 2022, **144**, 17033–17040.

38 Y. Shi, S. Wang, W. Tao, J. Guo, S. Xie, Y. Ding, G. Xu, C. Chen, X. Sun, Z. Zhang, Z. He, P. Wei and B. Z. Tang, *Nat. Commun.*, 2022, **13**, 1882.

39 Y. Shi, Y. Ding, W. Tao and P. Wei, *ACS Appl. Mater. Interfaces*, 2022, **14**, 36071–36078.

40 Y. Lv, D. Li, A. Ren, Z. Xiong, Y. Yao, K. Cai, S. Xiang, Z. Zhang and Y. S. Zhao, *ACS Appl. Mater. Interfaces*, 2021, **13**, 28662–28667.

41 L. Ma, Y. Xie, R. S. H. Khoo, H. Arman, B. Wang, W. Zhou, J. Zhang, R.-B. Lin and B. Chen, *Chem.–Eur. J.*, 2022, **28**, e202104269.

42 M. Liang, S. Hu, N. Zhou, Z. Liu, Q. Chen, X. Chen, X. Liu, C.-P. Li, J. Hao and P. Xue, *Small*, 2023, 2304340.

43 L. Gong, Y. Ye, Y. Liu, Y. Li, Z. Bao, S. Xiang, Z. Zhang and B. Chen, *ACS Appl. Mater. Interfaces*, 2022, **14**, 19623–19628.

44 W.-G. Lee, T.-U. Yoon, Y.-S. Bae, K. S. Kim and S. B. Baek, *RSC Adv.*, 2019, **9**, 36808–36814.

45 F.-A. Guo, K. Zhou, J. Liu, H. Wang and J. Li, *Precis. Chem.*, 2023, DOI: 10.1021/prechem.1023c00040.

46 P. Ryan, O. K. Farha, L. J. Broadbelt and R. Q. Snurr, *AIChE J.*, 2011, **57**, 1759–1766.

47 B. J. Sikora, C. E. Wilmer, M. L. Greenfield and R. Q. Snurr, *Chem. Sci.*, 2012, **3**, 2217–2223.

48 X. Ding, Z. Liu, Y. Zhang, G. Ye, J. Jia and J. Chen, *Angew. Chem., Int. Ed.*, 2022, **61**, e202116483.

49 Y. Zhou, C. Chen, R. Krishna, Z. Ji, D. Yuan and M. Wu, *Angew. Chem., Int. Ed.*, 2023, **62**, e202305041.

50 Y. Cai, J. Gao, J.-H. Li, P. Liu, Y. Zheng, W. Zhou, H. Wu, L. Li, R.-B. Lin and B. Chen, *Angew. Chem., Int. Ed.*, 2023, e202308579.

51 F. Zheng, L. Guo, R. Chen, L. Chen, Z. Zhang, Q. Yang, Y. Yang, B. Su, Q. Ren and Z. Bao, *Angew. Chem., Int. Ed.*, 2022, **61**, e202116686.

52 L. Li, L. Guo, Z. Zhang, Q. Yang, Y. Yang, Z. Bao, Q. Ren and J. Li, *J. Am. Chem. Soc.*, 2019, **141**, 9358–9364.

53 L. Gong, Y. Liu, J. Ren, A. M. Al-Enizi, A. Nafady, Y. Ye, Z. Bao and S. Ma, *Nano Res.*, 2022, **15**, 7559–7564.

54 M. H. Mohamed, S. K. Elsaidi, T. Pham, K. A. Forrest, H. T. Schaef, A. Hogan, L. Wojtas, W. Xu, B. Space, M. J. Zaworotko and P. K. Thallapally, *Angew. Chem., Int. Ed.*, 2016, **55**, 8285–8289.

55 K. B. Idrees, Z. Chen, X. Zhang, M. R. Mian, R. J. Drout, T. Islamoglu and O. K. Farha, *Chem. Mater.*, 2020, **32**, 3776–3782.

56 Y. Liu, J. Dai, L. Guo, Z. Zhang, Y. Yang, Q. Yang, Q. Ren and Z. Bao, *CCS Chem.*, 2022, **4**, 381–388.

57 S. Xiong, Y. Gong, S. Hu, X. Wu, W. Li, Y. He, B. Chen and X. Wang, *J. Mater. Chem. A*, 2018, **6**, 4752–4758.

58 Z. Niu, Z. Fan, T. Pham, G. Verma, K. A. Forrest, B. Space, P. K. Thallapally, A. M. Al-Enizi and S. Ma, *Angew. Chem., Int. Ed.*, 2022, **61**, e202117807.

59 W. Gong, Y. Xie, X. Wang, K. O. Kirlikovali, K. B. Idrees, F. Sha, H. Xie, Y. Liu, B. Chen, Y. Cui and O. K. Farha, *J. Am. Chem. Soc.*, 2023, **145**, 2679–2689.

60 H. Wang, Z. Shi, J. Yang, T. Sun, B. Rungtaweevoranit, H. Lyu, Y.-B. Zhang and O. M. Yaghi, *Angew. Chem., Int. Ed.*, 2021, **60**, 3417–3421.

61 W. Gong, Y. Xie, T. D. Pham, S. Shetty, F. A. Son, K. B. Idrees, Z. Chen, H. Xie, Y. Liu, R. Q. Snurr, B. Chen, B. Alameddine, Y. Cui and O. K. Farha, *J. Am. Chem. Soc.*, 2022, **144**, 3737–3745.

62 X. Song, Q. Huang, J. Liu, H. Xie, K. B. Idrees, S. Hou, L. Yu, X. Wang, F. Liu, Z. Qiao, H. Wang, Y. Chen, Z. Li and O. K. Farha, *ACS Appl. Mater. Interfaces*, 2023, **15**, 18229–18235.

63 Z. Yan, Y. Gong, B. Chen, X. Wu, Q. liu, L. Cui, S. Xiong and S. Peng, *Sep. Purif. Technol.*, 2020, **239**, 116514.

64 Q. Wang, S. Xiong, Z. Xiang, S. Peng, X. Wang and D. Cao, *Sci. China: Chem.*, 2016, **59**, 643–650.

65 P. R. Spackman, M. J. Turner, J. J. McKinnon, S. K. Wolff, D. J. Grimwood, D. Jayatilaka and M. A. Spackman, *J. Appl. Crystallogr.*, 2021, **54**, 1006–1011.

This journal is © The Royal Society of Chemistry 2023

J. Mater. Chem. A, 2023, **11**, 21857–21863 | **21863**